

# Covalent Organic Framework Membranes with Asymmetric Wettability for Efficient Photocatalytic H<sub>2</sub>O<sub>2</sub> Synthesis

Chi Qiao<sup>+</sup>, Weipeng Xian<sup>+</sup>, Zhuozhi Lai, Zhirou Huang, Qing Guo, Sai Wang, Zhifeng Dai,\*  
Yubing Xiong, Xiangju Meng,\* Shengqian Ma, and Qi Sun\*

**Abstract:** Photocatalytic H<sub>2</sub>O<sub>2</sub> synthesis from air and water is a sustainable route but hindered by mass transport and charge separation issues. Here, covalent organic framework (COF) membranes with asymmetric wettability are developed to construct triphase interfaces, locally enriching O<sub>2</sub> and H<sub>2</sub>O for efficient reactions. Converting COF powders into nanostructured membranes enhances light absorption and band alignment, promoting water oxidation and charge separation. These synergistic effects boost H<sub>2</sub>O<sub>2</sub> production to 52.5 mmol g<sup>-1</sup> h<sup>-1</sup> under O<sub>2</sub>, with an apparent quantum yield 27.8 times higher than powders, and up to 148.9-fold under air. The flexible membranes can be integrated into reactors, and the in situ generated H<sub>2</sub>O<sub>2</sub> enables pollutant degradation. This work demonstrates a versatile strategy for high-performance triphase photocatalysis and multifunctional membrane catalysts toward sustainable chemical synthesis.

## Introduction

The escalating global energy crisis and environmental degradation underscore the urgent need for sustainable solutions, positioning H<sub>2</sub>O<sub>2</sub> as a cornerstone of green technology. H<sub>2</sub>O<sub>2</sub> offers compelling advantages, such as a high energy density (3.0 MJ L<sup>-1</sup>), stable storage properties, and versatile applications, ranging from eco-friendly pollutant degradation to sustainable chemical synthesis.<sup>[1–5]</sup> Despite market projections forecasting a 4.6% annual growth rate, with demand expected to reach 5.7 million metric tons by 2028, the current industrial H<sub>2</sub>O<sub>2</sub> production remains reliant on the energy-

intensive anthraquinone process, which imposes substantial environmental burdens.<sup>[6–8]</sup> Therefore, solar-driven photocatalytic synthesis of H<sub>2</sub>O<sub>2</sub> from water and air has emerged as a promising alternative, offering a renewable solution to these challenges.<sup>[9–12]</sup> Recent developments in photocatalysis have focused on material strategies such as band structure engineering and charge carrier modulation.<sup>[13–25]</sup> However, significant challenges remain, particularly in maximizing light utilization and overcoming mass transfer limitations in gas-liquid-solid (triphase) reaction systems. Conventional systems that use suspended catalysts in aqueous media face inherent limitations, including the low solubility of O<sub>2</sub>, which is constrained by Henry's law (9 mg L<sup>-1</sup> at 1 atm, 20 °C), and slow O<sub>2</sub> diffusion rates in water ( $D = 2 \times 10^{-5}$  cm<sup>2</sup> s<sup>-1</sup>), both of which hinder reaction kinetics. At gas-liquid interfaces, however, where O<sub>2</sub> concentration and diffusivity increase to 8.7 μmol mL<sup>-1</sup> and  $2 \times 10^{-1}$  cm<sup>2</sup> s<sup>-1</sup>, respectively, there is a 35-fold increase in concentration and a 10000-fold enhancement in diffusivity compared to bulk aqueous phases.<sup>[26–30]</sup> This stark contrast underscores the transformative potential of catalytic systems that optimize mass transfer.

Membrane-based photocatalytic systems offer significant advantages by enhancing light utilization and addressing challenges in interfacial engineering.<sup>[31–33]</sup> These systems allow for precise control over wettability, enabling customization for specific reaction environments.<sup>[34,35]</sup> Among various membrane materials, covalent organic frameworks (COFs) are particularly promising due to their periodic arrangement of electron donor-acceptor units, which facilitate efficient charge separation upon photoexcitation. Moreover, the long-range ordered structures of 2D COFs enable rapid transport of photogenerated excitons, thereby minimizing recombination losses.<sup>[36–51]</sup> We propose engineering bulk COFs into membranes with asymmetric wettability, which synergistically combines wettability-guided O<sub>2</sub> and H<sub>2</sub>O delivery with

[\*] C. Qiao<sup>+</sup>, Prof. Z. Dai, Prof. Y. Xiong  
Key Laboratory of Surface & Interface Science of Polymer Materials of Zhejiang Province, School of Chemistry and Chemical Engineering, Zhejiang Sci-Tech University, Hangzhou 310018, China  
E-mail: [daizhifeng1988@163.com](mailto:daizhifeng1988@163.com)


C. Qiao<sup>+</sup>, W. Xian<sup>+</sup>, Z. Lai, Q. Guo, Prof. Q. Sun  
Key Laboratory of Biomass Chemical Engineering of Ministry of Education, College of Chemical and Biological Engineering, Zhejiang University, Hangzhou 310058, China  
E-mail: [sunqichs@zju.edu.cn](mailto:sunqichs@zju.edu.cn)

Z. Huang, Prof. S. Wang  
Hangzhou Institute of Advanced Studies, Zhejiang Normal University, Hangzhou 310015, China

Prof. X. Meng  
Department of Chemistry, Zhejiang University, Hangzhou 310027, China  
E-mail: [mengxj@zju.edu.cn](mailto:mengxj@zju.edu.cn)

Prof. S. Ma  
Department of Chemistry, University of North Texas, 1508 W Mulberry St Denton, TX 76201, USA

[+] Both authors contributed equally to this work.

 Additional supporting information can be found online in the Supporting Information section

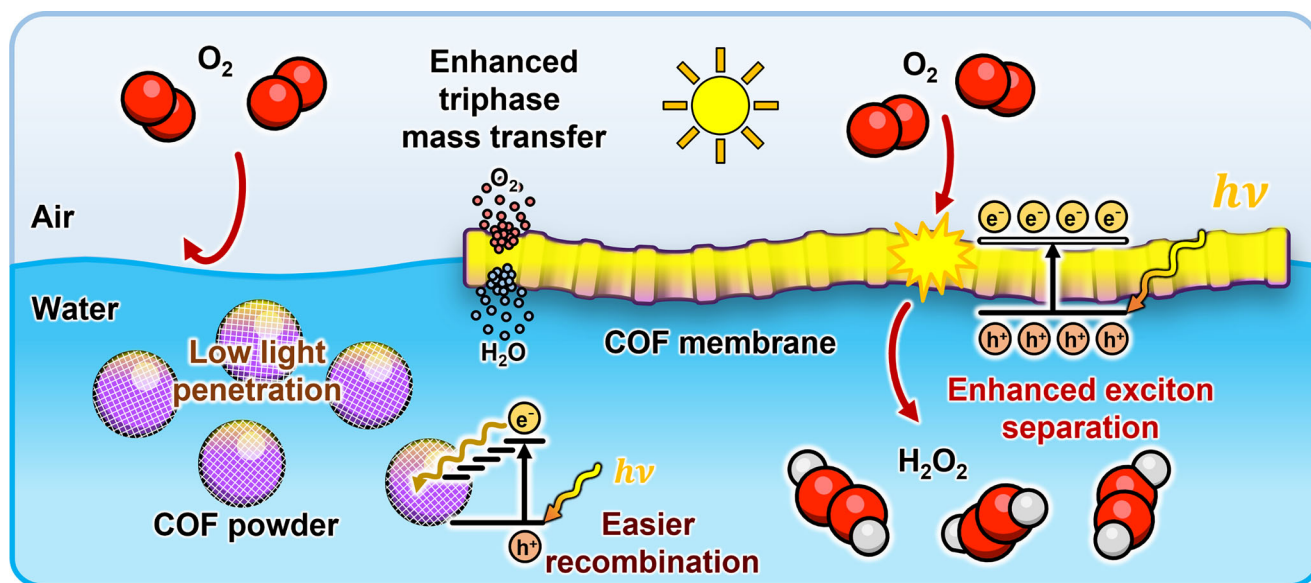


**Figure 1.** Comparison of COF powder and COF membrane with asymmetric wettability for enhanced  $\text{H}_2\text{O}_2$  production. The asymmetric wettability of the membrane creates a gas-liquid-solid reaction interface, facilitating localized  $\text{O}_2$  enrichment and efficient reactant diffusion. In contrast, the powdered system is limited by poor  $\text{O}_2$  accessibility and bulk-phase reaction constraints. Additionally, the membrane structure enhances exciton separation, further optimizing the photocatalytic process.

built-in charge separation pathways, while enhancing light penetration efficiency to improve catalytic performance. In addition to these, fabricating COF powders into seamless, oriented membranes reduces structural defects, shortens charge migration distances, and optimizes band structures, all expected to enhance photocatalytic performance (Figure 1).<sup>[52–56]</sup>

To realize this concept, we selected imine-linked COF membranes for their high crystallinity and unique ability to modulate wettability by adjusting the protonation degree of their imine bonds.<sup>[57,58]</sup> Specifically, higher protonation degrees increase hydrophilicity. This hierarchical structure addresses key interfacial engineering challenges: the hydrophobic surface ensures a continuous atmospheric  $\text{O}_2$  supply, while the hydrophilic layer maximizes contact with aqueous reactants, creating an integrated gas-liquid-solid triphase reaction zone. Moreover, constructing ultrathin COF membranes not only enhances exciton separation but also improves photoreactivity. These advances yielded a record  $\text{H}_2\text{O}_2$  production rate of  $12.5 \text{ mmol g}^{-1} \text{ h}^{-1}$  under natural sunlight ( $98 \text{ mW cm}^{-2}$ , ambient air) and  $52.5 \text{ mmol g}^{-1} \text{ h}^{-1}$  under simulated sunlight ( $300 \text{ mW cm}^{-2}$ , Xe lamp,  $\text{O}_2$  atmosphere), positioning this system among the highest-performing catalysts under comparable conditions (Table S1). The free-standing membrane design allows facile integration into diverse reactor configurations, enabling efficient organic pollutant degradation via in situ-generated  $\text{H}_2\text{O}_2$ . This work presents a transformative approach to photocatalytic membrane reactors, enhancing both processability and catalytic performance through strategic material and interfacial engineering.

## Results and Discussion

### Membrane Synthesis and Characterizations

Leveraging the strong light-absorption capability of porphyrin moieties and the potential of hydroxyl-functionalized monomers as proton reservoirs for enhanced  $\text{H}_2\text{O}_2$  production,<sup>[59–62]</sup> we synthesized a series of COF membranes by pairing 4,4',4'',4'''-(porphyrin-5,10,15,20-tetrayl)tetraaniline (Pta) with 2,5-dihydroxyterephthalaldehyde (Dha) as a proof-of-concept. By varying the concentrations of Pta in aqueous acetic acid and Dha in an ethyl acetate-mesitylene mixture, we successfully fabricated robust, purple-colored membranes with areas up to  $600 \text{ cm}^2$  ( $20 \times 30 \text{ cm}$ ) (Figure 2a,b, inset). This liquid-liquid interfacial polymerization strategy promoted nucleation at the interface, effectively suppressing random precipitation. The confined 2D reaction environment favored the formation of continuous and uniform membranes, where porphyrin units preferentially aligned with their  $\pi$ - $\pi$  stacking direction parallel to the interface, minimizing interfacial energy and driving the formation of 1D channels oriented perpendicular to the substrate. Once nucleation occurred, epitaxial growth propagated this vertical channel alignment across the entire membrane. Atomic force microscopy (AFM) confirmed that decreasing monomer concentrations led to thinner membranes, with thicknesses ranging from  $140 \text{ nm}$  (COF-M140) to  $650 \text{ nm}$  (COF-M650) (Figures S1–S4). Accordingly, the membranes were designated COF-M140, COF-M180, COF-M300, and COF-M650 based on their measured thicknesses. Distinct optical properties were

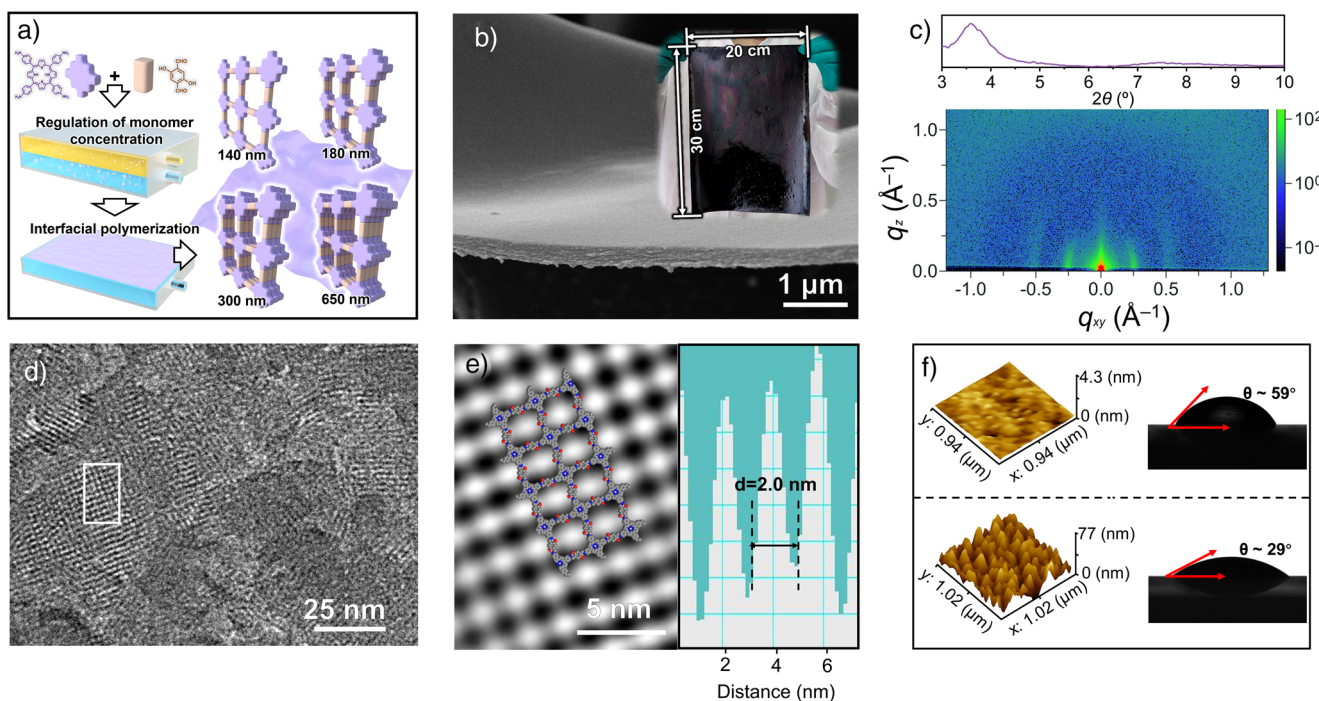


**Figure 2.** Membrane synthesis and characterization. a) Schematic illustration of the acid-catalyzed liquid-liquid interfacial polymerization used to fabricate COF membranes with varying thicknesses by adjusting the monomer concentration. b) SEM image of COF-M180 (inset: photograph of COF-M180 after being transferred onto a polyacrylonitrile ultrafiltration membrane, with dimensions of 20 cm by 30 cm). c) GIWAXS pattern of the COF-M180 membrane. d) TEM image of COF-M180, highlighting their high crystallinity. e) Lattice fringe image obtained from the inverse fast Fourier transform of the square-framed region in panel d), along with the corresponding average intensity profiles. f) AFM surface image showing the average roughness and water contact angles for both the organic-facing side (top) and aqueous-facing side (bottom).

observed depending on the membrane surface: the organic-facing side exhibited a glossy, mirror-like purple appearance, while the aqueous-facing side appeared matte with minimal reflectivity (Figure S5). Scanning electron microscopy (SEM) confirmed a seamless, defect-free morphology, free of cracks or pinholes (Figures 2b, and S1–S4). Structural analysis using 2D grazing-incidence wide-angle X-ray scattering (GIWAXS) revealed in-plane diffraction peaks, indicating the oriented growth of 2D COF layers with pores aligned perpendicular to the substrate. The 1D projections of the GIWAXS patterns corresponded to an eclipsed AA-stacking configuration, consistent with the crystallinity of solvothermally synthesized COF powder and confirmed by simulated diffraction patterns. Pawley refinements of the powder X-ray diffraction (PXRD) patterns of the membranes were performed for full-profile fitting against the proposed AA-stacking model, yielding good agreement factors ( $R_{WP} = 2.47\%$  after convergence) and reasonable profile differences (Figures 2c, S6, and S7). Transmission electron microscopy (TEM) further supported the ordered architecture, revealing large crystalline domains with square-shaped pores ( $\sim 2.0$  nm diameter) or 1D channels, depending on the imaging orientation (Figures 2d,e, and S8–S10).  $N_2$  sorption isotherms at 77 K confirmed the porosity of membranes, with the COF-M180 membrane exhibiting a Brunauer–Emmett–Teller (BET) surface area of  $355 \text{ m}^2 \text{ g}^{-1}$  and a pore size distribution centered at 1.8 nm (Figure S11).

To evaluate the surface properties and wettability, we measured the water contact angle (WCA) on both the

aqueous- and organic-facing sides of membranes with varying thicknesses. Significant differences were observed between the two sides. The aqueous-facing side exhibited much higher hydrophilicity compared to the organic-facing side. As membrane thickness decreased, hydrophilicity increased, with the WCA dropping from  $47^\circ$  for COF-M650 to  $20^\circ$  for COF-M140. In contrast, the organic-facing side remained consistently hydrophobic, with WCA values ranging from  $59^\circ$  to  $66^\circ$ , regardless of membrane thickness (Figures 2f and S12). AFM analysis of surface morphology revealed structural asymmetry that the hydrophobic organic-facing side displayed a smooth, uniform topography with minimal folding (average roughness,  $R_a < 0.53$  nm), while the hydrophilic aqueous-facing side exhibited more pronounced fluctuations and irregularities. The  $R_a$  values for the aqueous side increased with membrane thickness, ranging from 4.4 nm (COF-M140) to 12 nm (COF-M650). This contrast supports the Wenzel wettability model, which suggests that surface roughness enhances the intrinsic wettability determined by surface chemistry.<sup>[63]</sup>

These findings suggest that the observed differences in wettability originate from side-specific chemical compositions. To further investigate this, Fourier-transform infrared (FT-IR) spectroscopy was conducted on both the aqueous-facing and organic-facing sides of the membranes. The spectra revealed nearly complete consumption of the monomeric amino ( $-\text{NH}_2$ ) and aldehyde ( $-\text{CHO}$ ) groups, accompanied by the emergence of characteristic imine ( $-\text{C}=\text{N}-$ ) stretching

bands around  $\sim 1613\text{ cm}^{-1}$ , confirming the successful Schiff-base condensation reaction.<sup>[64,65]</sup> In addition, residual acetate-related signals were detected in all membranes, characterized by C=O stretching ( $\sim 1738\text{ cm}^{-1}$ ) and C–H stretching of methyl groups ( $\sim 2921\text{ cm}^{-1}$ ) (Figures S13–S15).<sup>[66]</sup> These acetate signals were further corroborated by solid-state  $^{13}\text{C}$  NMR spectroscopy (Figure S16). Interestingly, the intensity of the acetate signals exhibited thickness- and side-dependent trends, with thinner membranes displaying stronger peaks, and the aqueous-facing side showing higher signal intensity compared to the organic-facing side. In contrast, the thicker COF-M650 membrane retained acetate signals only on its aqueous-facing side. To rule out the possibility of infrared penetration artifacts influencing the detection of acetate on both sides, X-ray photoelectron spectroscopy (XPS) was employed to probe the surface chemistry within a depth of less than 10 nm. XPS analysis revealed side-specific protonation differences, with thinner membranes showing higher protonation levels of N species on the aqueous-facing side, while the organic-facing side remained predominantly unprotonated.<sup>[67]</sup> This trend closely aligned with the hydrophilicity measurements (Figures S17 and S18).

Considering the pKa of acetic acid (pKa = 4.7) lies between those of the imine linkages (pKa  $\approx$  7.0) and the porphyrin moieties (pKa = 3.65 and 3.81), the detected protonated N species are attributed to protonated imine linkages.<sup>[58]</sup> The observed protonation gradient across the COF membrane can be explained by the formation mechanism during acid-catalyzed liquid-liquid interfacial polymerization. The membrane nucleates at the water-oil interface and gradually grows outward from the aqueous phase toward the organic phase. As the distance from the acidic aqueous phase increases, the degree of deprotonation rises, giving rise to a protonation gradient across the membrane thickness. Because the COF membrane is less dense than water, thicker membranes extend further into the organic phase, resulting in a lower overall protonation level. A similar phenomenon was observed in our previous work (Figure S19).<sup>[67]</sup> This controllably engineered asymmetric hydrophobicity is expected to be advantageous for photocatalytic  $\text{H}_2\text{O}_2$  production. The hydrophobic organic face facilitates efficient  $\text{O}_2$  transport into the membrane pore channels, while the hydrophilic aqueous face ensures strong interactions with  $\text{H}_2\text{O}$ , thus synergistically enhancing reaction efficiency.

### Photocatalytic $\text{H}_2\text{O}_2$ Performance Evaluation

After synthesizing COF membranes with varying asymmetric wettability, along with their powdered counterpart (COF-P), we systematically evaluated their photocatalytic performance for  $\text{H}_2\text{O}_2$  generation (Figures S20–S22). The experiments were conducted in deionized water under ambient atmospheric conditions, without the use of sacrificial agents or cocatalysts, using a Xe lamp ( $200\text{ mW cm}^{-2}$ ) as the light source. It is well known that the yield of  $\text{H}_2\text{O}_2$  is highly dependent on its concentration in solution, as excessive accumulation can inhibit further generation. To ensure a fair comparison, the catalyst-to-water ratio was kept constant in all experiments,

irrespective of whether the catalyst was used in membrane or powder form.<sup>[68]</sup> The  $\text{H}_2\text{O}_2$  production rates exhibited a volcano-shaped dependence on membrane thickness, peaking at  $26.78\text{ mmol g}^{-1}\text{ h}^{-1}$  for COF-M180, which represents a 148.9-fold enhancement compared to the powdered catalyst ( $0.18\text{ mmol g}^{-1}\text{ h}^{-1}$ , Figure 3a). Notably, COF-M180 showed a linear increase in  $\text{H}_2\text{O}_2$  production with increasing light intensity, achieving  $38.0\text{ mmol g}^{-1}\text{ h}^{-1}$  at  $300\text{ mW cm}^{-2}$ . Under natural sunlight, COF-M180 maintained a production rate of  $12.5\text{ mmol g}^{-1}\text{ h}^{-1}$  (Figures S23 and S24). To assess practical viability, COF-M180 was tested in natural water sources (lake, river, seawater, and tap water), retaining 76.4%–101.2% of its  $\text{H}_2\text{O}_2$  production efficiency observed in deionized water (Figure S25). This minimal decline in performance highlights the robustness of the membranes in complex aqueous environments and underscores their potential for real-world applications.

### Mechanistic Insights into Enhanced Catalytic Efficiency

To better understand the significant efficiency disparity between COF membranes and COF-P, we examined the mass transfer dynamics. While the COF membranes floated at the gas-liquid interface, COF-P was fully submerged in the aqueous phase (Figure 3b). Given the triphase nature of the reaction, we hypothesized that the interfacial positioning of the membranes provides direct access to atmospheric  $\text{O}_2$ , thereby significantly enhancing mass transfer. This hypothesis was further supported when acetone was introduced into the reaction system, causing the floating COF membrane to sink and triggering visible gas release. High-frame-rate camera footage captured the gas release during the  $\text{H}_2\text{O}$ -acetone displacement (Figure 3c). Furthermore,  $\text{O}_2$  temperature-programmed desorption ( $\text{O}_2$ -TPD) analysis confirmed the clear physical adsorption capacity of the COF-M180 membrane for  $\text{O}_2$  (Figure S26). We propose that the efficiency differences among membranes of varying thicknesses are related to their interfacial distribution, which governs  $\text{O}_2$  diffusion and  $\text{H}_2\text{O}$  availability. To test this, the membranes were ground into powders and their performance was reassessed in aqueous dispersion. The  $\text{H}_2\text{O}_2$  production rates for the powdered COF membranes decreased to 8.76, 10.77, 9.85, and  $6.44\text{ mmol g}^{-1}\text{ h}^{-1}$  for COF-M140, COF-M180, COF-M300, and COF-M650, respectively, narrowing the performance gap observed with intact membranes (Figure 3d). Further validation of the importance of interfacial  $\text{O}_2$  transfer was carried out using COF-M180, the highest-performing membrane, as a model. When the membrane was inverted, orienting the hydrophobic side toward the water and the hydrophilic side toward the air, the  $\text{H}_2\text{O}_2$  production rate was halved, decreasing from  $26.78$  to  $13.76\text{ mmol g}^{-1}\text{ h}^{-1}$  (Figure S27).

Additionally, replacing ambient air with pure  $\text{O}_2$  resulted in a 1.5-fold increase in  $\text{H}_2\text{O}_2$  production compared to air-saturated conditions. In contrast, the powdered COF-M180 membrane and COF-P demonstrated 2.2-fold and 7.1-fold higher  $\text{H}_2\text{O}_2$  production rates, respectively, under  $\text{O}_2$  saturated conditions compared to air-saturated systems (Figure 3e). Under  $300\text{ mW cm}^{-2}$  Xe lamp illumination

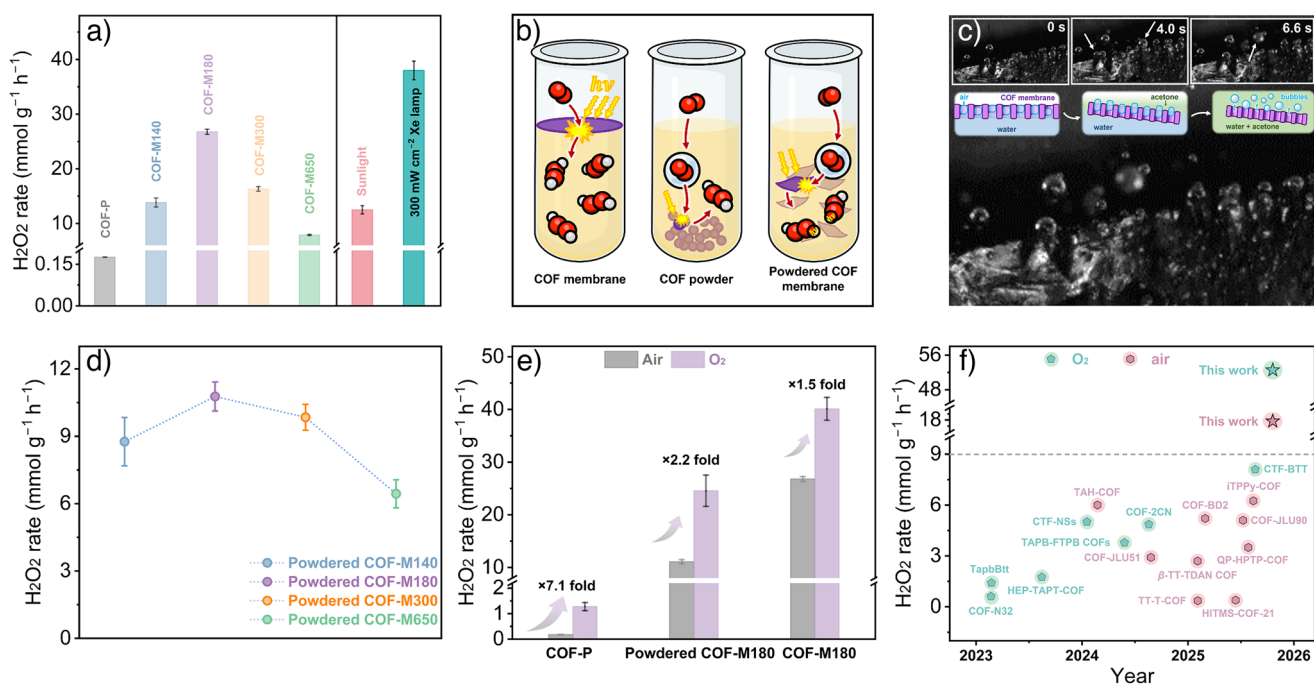


**Figure 3.** Comparison of photocatalytic  $\text{H}_2\text{O}_2$  production across various systems. a) Comparison of  $\text{H}_2\text{O}_2$  production rates for different catalytic systems after 1 h under a  $200 \text{ mW cm}^{-2}$  Xe lamp with ambient air (left), and the  $\text{H}_2\text{O}_2$  production rate of COF-M180 under natural sunlight and air conditions, as well as under a  $300 \text{ mW cm}^{-2}$  Xe lamp with an  $\text{O}_2$  atmosphere. b) Schematic illustration of  $\text{O}_2$  mass transport and light penetration in various catalytic systems. c) Photographs showing the gas release process from COF membranes (inset: schematic illustrating the observation of gas release from the membrane floating on the water surface, using acetone replacement and captured by a high-frame rate camera at 200 frames per second). d) Comparison of  $\text{H}_2\text{O}_2$  production rates across different powdered COF membranes after 1 h under a  $200 \text{ mW cm}^{-2}$  Xe lamp with ambient air conditions. e) Comparison of  $\text{H}_2\text{O}_2$  production rates for various catalysts after 1 h under a  $200 \text{ mW cm}^{-2}$  Xe lamp in air and  $\text{O}_2$  atmospheres. f) Comparison of the COF-M180 membrane with other COF systems from Table S1 under a  $100 \text{ mW cm}^{-2}$  Xe lamp, except for the star with a green background, which corresponds to experiments performed under  $300 \text{ mW cm}^{-2}$ . Error bars represent the standard deviation from three independent trials for each catalytic system.

with pure  $\text{O}_2$ , COF-M180 achieved  $52.5 \text{ mmol g}^{-1} \text{ h}^{-1}$  of  $\text{H}_2\text{O}_2$  production, one of the highest rates reported for photocatalytic systems (Figure 3f). These findings underscore the crucial role of  $\text{O}_2$  availability and triphase interfacial engineering in enhancing mass transfer and photocatalytic efficiency.

Next, we investigated the mechanistic role of  $\text{O}_2$  through radical trapping experiments and electron transfer analysis. Previous studies suggest that  $\text{H}_2\text{O}_2$  synthesis primarily occurs via the  $\text{O}_2$  reduction reaction (ORR), involving intermediates such as superoxide anions ( $\bullet\text{O}_2^-$ ), hydroperoxyl radicals ( $\bullet\text{OOH}$ ), and singlet oxygen ( $^1\text{O}_2$ ).<sup>[69–73]</sup> The introduction of 10% (v/v) benzyl alcohol as an electron donor increased the  $\text{H}_2\text{O}_2$  production rate of COF-M180 to  $31.58 \text{ mmol g}^{-1} \text{ h}^{-1}$  under air, a 1.18-fold enhancement compared to the benzyl alcohol-free system (Figure 4a).<sup>[74,75]</sup> To further elucidate the  $\text{O}_2$  reduction pathway, electron paramagnetic resonance (EPR) spectroscopy using 5,5-dimethyl-1-pyrroline N-oxide (DMPO) as a spin trap revealed six-line peaks characteristic of DMPO- $\bullet\text{O}_2^-$  adducts (Figure 4b). Notably, the COF-M180 membrane at the gas-liquid interface exhibited significantly stronger  $\bullet\text{O}_2^-$  signals than the submerged COF-P, directly linking triphase  $\text{O}_2$  enrichment to enhanced  $\bullet\text{O}_2^-$  generation (Figure S28). Parallel experiments using 2,2,6,6-tetramethylpiperidine (TEMP) to trap  $^1\text{O}_2$  displayed a similar

trend.<sup>[76–80]</sup> Scavenger experiments were conducted to assess the contributions of reactive species. Adding *p*-benzoquinone (a  $\bullet\text{O}_2^-/\bullet\text{OOH}$  scavenger) reduced the  $\text{H}_2\text{O}_2$  production rate of COF-M180 from  $26.78$  to  $8.64 \text{ mmol g}^{-1} \text{ h}^{-1}$ , while  $\text{NaN}_3$  or 1,4-diazabicyclo[2.2.2]octane (DABCO,  $^1\text{O}_2$  scavengers) showed no inhibitory effect. Similarly, the  $\text{H}_2\text{O}_2$  yield of COF-P plummeted from  $0.18$  to  $0.008 \text{ mmol g}^{-1} \text{ h}^{-1}$  with *p*-benzoquinone but remained unaffected by  $\text{NaN}_3$  or DABCO (Figure S29). These results confirm that  $\bullet\text{O}_2^-$ , facilitated by  $\text{O}_2$  accessibility, is critical for  $\text{H}_2\text{O}_2$  synthesis, while  $^1\text{O}_2$  plays a negligible role in the reaction. Rotating ring-disk electrode (RRDE) tests further supported the two-electron ORR pathway ( $\text{O}_2 + 2e^- + 2\text{H}^+ \rightarrow \text{H}_2\text{O}_2$ ), with derived electron transfer numbers  $n \approx 2.18$  for COF-M180 and  $2.28$  for COF-P (Figure 4c). These values align with a stepwise single-electron transfer mechanism, consistent with the ability of triphase systems to sustain efficient ORR.<sup>[81–83]</sup> Finally, nitrotetrazolium blue chloride (NBT) assays quantified  $\bullet\text{O}_2^-$  production, showing a pronounced UV-vis absorbance decrease at  $275 \text{ nm}$  after illumination (Figures 4d and S30). The greater reduction observed for COF-M180 membrane compared to COF-P directly correlates with its superior  $\text{H}_2\text{O}_2$  yield, highlighting how the triphase interface amplifies reactive  $\text{O}_2$  species generation to maximize catalytic output.

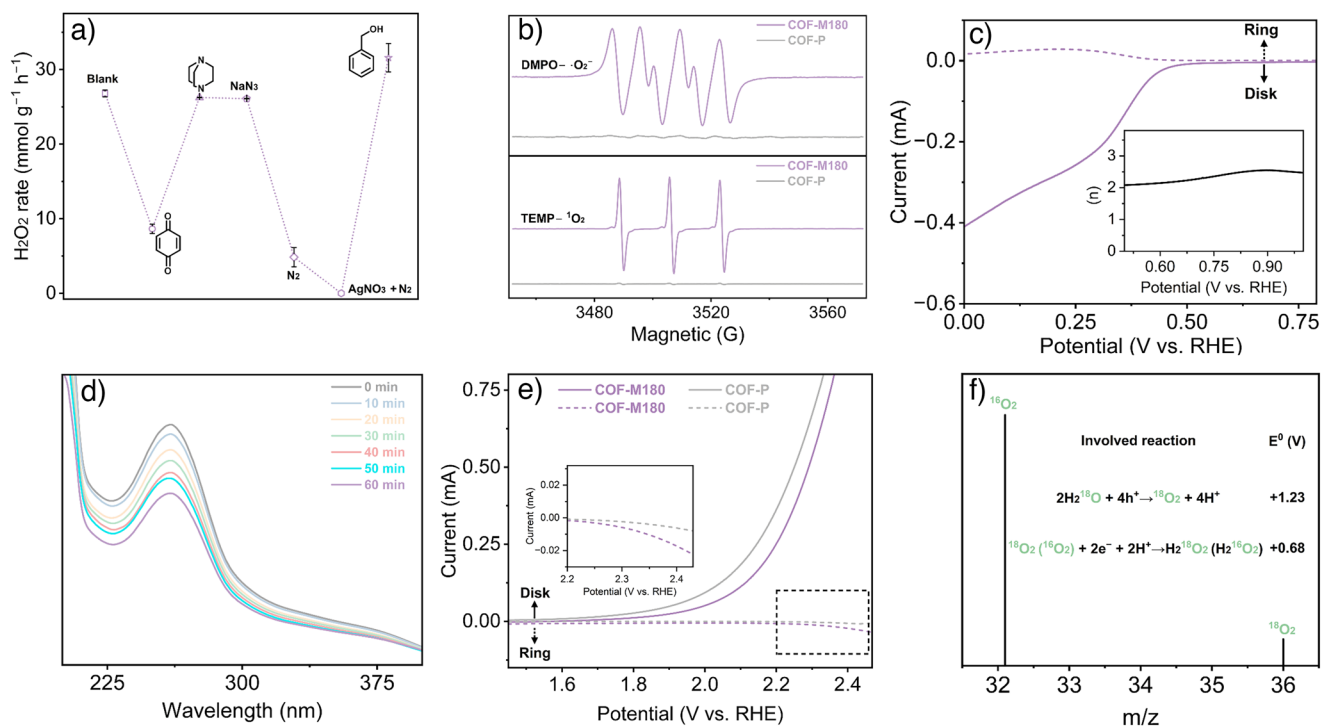


**Figure 4.** Mechanism of photocatalytic H<sub>2</sub>O<sub>2</sub> production. a) Photoactivity of COF-M180 in the presence of different scavengers. b) Comparison of EPR spectra of COF-M180 and COF-P under light illumination, using the spin-trapping agents DMPO and TEMP, respectively. c) Polarization curves recorded with simultaneous detection of H<sub>2</sub>O<sub>2</sub> at the ring electrode rotating at 1600 rpm. Inset: Electron transfer number calculated using the disk and ring currents from the RRDE. d) Time-dependent degradation of NBT to detect •O<sub>2</sub><sup>-</sup> generated by COF-M180. e) RRDE voltammograms obtained in 0.1 M phosphate buffer solution with a scan rate of 10 mV s<sup>-1</sup> and a rotation rate of 1600 rpm. The potential of the Pt ring electrode is set at -0.23 V versus Ag/AgCl to detect O<sub>2</sub>. Inset: Enlarged ring current spectra within the black dashed box. f) GC-MS analysis of the decomposed products from H<sub>2</sub>O<sub>2</sub> using the H<sub>2</sub><sup>18</sup>O isotope experiment, confirming that the COF-M180 membrane facilitates direct two-electron WOR, generating H<sub>2</sub><sup>18</sup>O<sub>2</sub>.

Subsequently, we investigated the residual activity of COF-M180 under N<sub>2</sub> conditions. After the removal of O<sub>2</sub>, the COF-M180 membrane retained some H<sub>2</sub>O<sub>2</sub> production (4.84 mmol g<sup>-1</sup> h<sup>-1</sup>), while COF-P exhibited negligible activity. This significant contrast led us to explore alternative pathways, particularly water oxidation (WOR). RRDE measurements revealed that the COF-M180 membrane facilitated WOR, generating O<sub>2</sub>, while the powdered catalyst showed no activity (Figure 4e). Isotopic labeling experiments using H<sub>2</sub><sup>18</sup>O confirmed the production of <sup>18</sup>O<sub>2</sub> for COF-M180, which was detected at *m/z* = 36 via mass spectrometry (Figure 4f). This suggests that O<sub>2</sub> produced through WOR is retained within the membrane triphase interface, where it subsequently contributes to the ORR pathway, sustaining H<sub>2</sub>O<sub>2</sub> synthesis. Further confirmation came from adding AgNO<sub>3</sub> (an electron scavenger) under N<sub>2</sub> conditions, which completely suppressed H<sub>2</sub>O<sub>2</sub> production.

To investigate the differing reactivity between the COF-M180 membrane and COF-P, we analyzed their optoelectronic characteristics. Solid-state UV-vis spectroscopy showed similar absorption edges for both materials. However, COF-P exhibited a more pronounced and intense absorption tail, likely due to enhanced light harvesting facilitated by tighter intermolecular  $\pi$ - $\pi$  stacking (Figure 5a).<sup>[74,75]</sup> Tauc plot analysis revealed nearly identical optical band gaps (1.72 eV for COF-P and 1.74 eV for COF-M180), indicating minimal differences in intrinsic light absorption (Figure 5a,

inset). Mott-Schottky-derived band positions highlighted key differences: the COF-M180 membrane had a valence band (VB) potential of 1.41 eV (versus NHE), surpassing the thermodynamic threshold for direct two-electron water oxidation reactions (1.23 V versus NHE). In contrast, the VB for COF-P was 1.16 eV, falling below this critical threshold (Figure S31). This subtle yet important shift in band alignment, driven by the morphological configuration of the membrane, thermodynamically supports its integrated water oxidation-reduction reaction (WOR-ORR) pathway (Figures 5b, S32, and S33). To further investigate the enhanced efficiency of COF-M180, we examined charge carrier dynamics through photoelectrochemical measurements. Temperature-dependent photoluminescence (PL) studies revealed that the PL emission intensities for both COF-M180 and COF-P decreased monotonically as the temperature increased from 75 to 290 K, consistent with thermally activated nonradiative recombination under resonant excitation (Figure 5c,d). Notably, the exciton binding energy (*E<sub>b</sub>*) of COF-M180 was calculated to be 75.5 meV, significantly lower than that of COF-P (136.9 meV), suggesting more efficient exciton dissociation into free charge carriers in the COF-M180 membrane. Electrochemical impedance spectroscopy (EIS) further confirmed enhanced charge transfer in the membrane, as evidenced by a smaller Nyquist plot arc radius compared to COF-P, indicating reduced interfacial charge-transfer resistance and more efficient charge migration (Figure 5e). Photocurrent

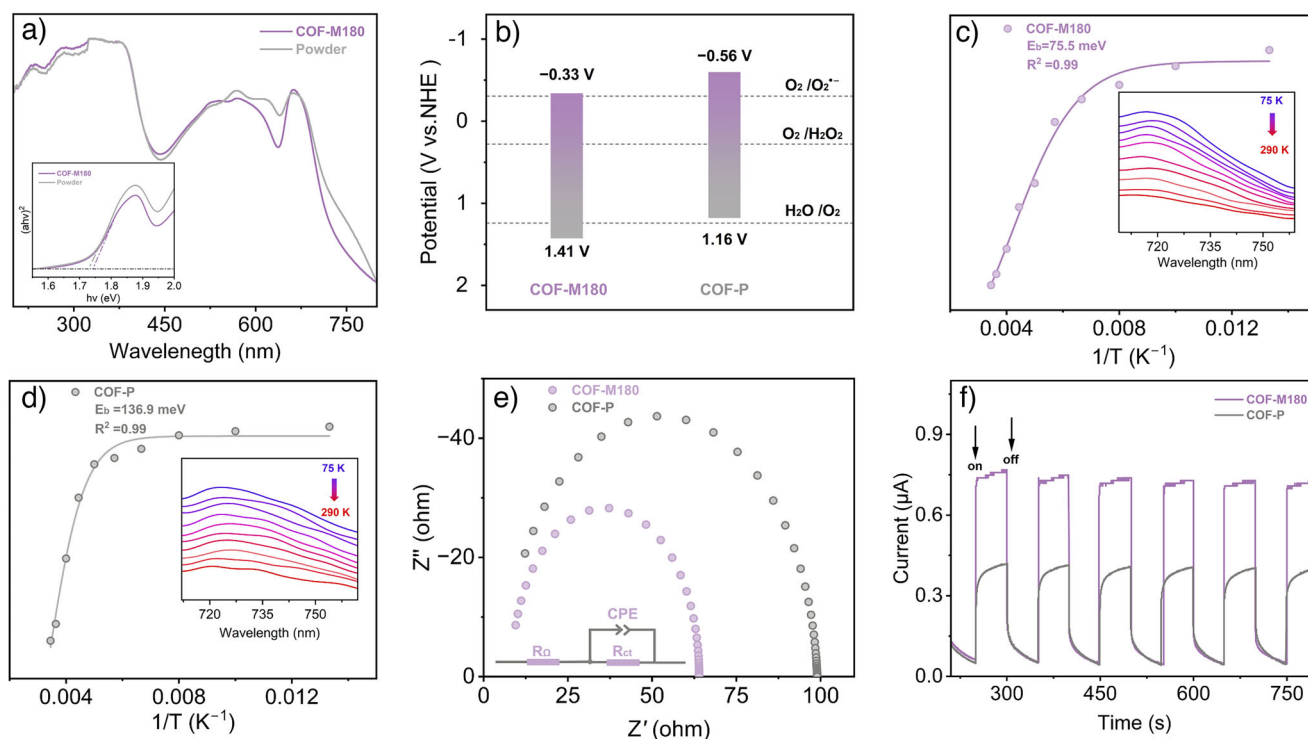


**Figure 5.** Comparison of optoelectronic characteristics between COF-M180 and COF-P. a) Solid-state UV-vis absorption spectra. Inset: Corresponding Tauc plots. b) Band structure diagram. c) Temperature-dependent integrated PL intensity for COF-M180 and d) COF-P, with extracted exciton binding energies. Inset: Emission spectra at different temperatures. e) EIS Nyquist plots in 0.1 M Na<sub>2</sub>SO<sub>4</sub> solution, recorded over a frequency range of 21 Hz to 100 kHz. Inset: Electrical equivalent circuit model used to simulate the EIS data.  $R_{\Omega}$ : solution resistance; CPE: constant phase element for the double-layer capacitance;  $R_{CT}$ : charge transfer resistance at the electrode/electrolyte interface. f) Photocurrent response measurements of COF-M180 and COF-P under 100 mW cm<sup>-2</sup> Xe lamp illumination.

density measurements supported this trend, with the COF-M180 membrane generating nearly double the photocurrent of COF-P (Figure 5f). Collectively, these results demonstrate that the structural configuration of COF-M180 optimizes its band structure, enabling superior charge separation and significantly enhancing its photocatalytic performance.

### Construction of Membrane Reactor for Organic Pollutant Degradation

Building on these promising results, we investigated the practical application of COF membranes for photocatalytic H<sub>2</sub>O<sub>2</sub> synthesis in the degradation of trace organic pollutants in water. Using Rhodamine B as a model pollutant, the COF membrane exhibited rapid degradation, reducing dye concentration by 50% within 1 h and achieving complete degradation within 3 h. In contrast, under the same conditions, COF-P reached only about 50% degradation after 10 h and failed to achieve full degradation even after 20 h (Figure S34). Importantly, the flexibility of COF membranes allows for easy integration into various reactor configurations (Figure 6a), such as tubular and flat-sheet membrane reactors, facilitating continuous and scalable organic pollutant degradation. Specifically, the COF-M180 and Al<sub>2</sub>O<sub>3</sub> composite membrane completely decomposed both Rhodamine B and tetracycline hydrochloride (25 mL, 2 ppm) within 3 h using the setup

shown in (Figure 6a-c). Additionally, a flat-sheet membrane reactor (Figures S35 and S36), assembled by attaching a COF-M180 membrane (3 cm × 3.5 cm) to a cellulose acetate support, achieved complete degradation of Rhodamine B (2 mg L<sup>-1</sup>) at a flow rate of 1 mL h<sup>-1</sup> after a single pass (Figure S37). The membrane reactor also continuously generated H<sub>2</sub>O<sub>2</sub>, with an average concentration of 1.75 mmol L<sup>-1</sup> after a single pass during a continuous 12-h run. Furthermore, the crystal structure of the membrane was preserved after catalysis, as confirmed by TEM analysis (Figures S38 and S39).

### Conclusion

In summary, this study highlights the transformative potential of COF membrane engineering in enhancing photocatalytic performance, offering a clear blueprint for the development of highly efficient photocatalytic membrane reactors. The presented system addresses three key challenges in the field: 1) improving triphase mass transfer at the reaction interface, 2) enhancing light penetration through nanostructured morphology, and 3) increasing reactivity through tailored band alignment and optimized exciton separation. Additionally, COF membranes facilitate seamless integration into various membrane reactors for continuous catalysis, utilizing in situ-generated H<sub>2</sub>O<sub>2</sub> for efficient organic degradation, offering a significant advantage over conventional batch reactors.

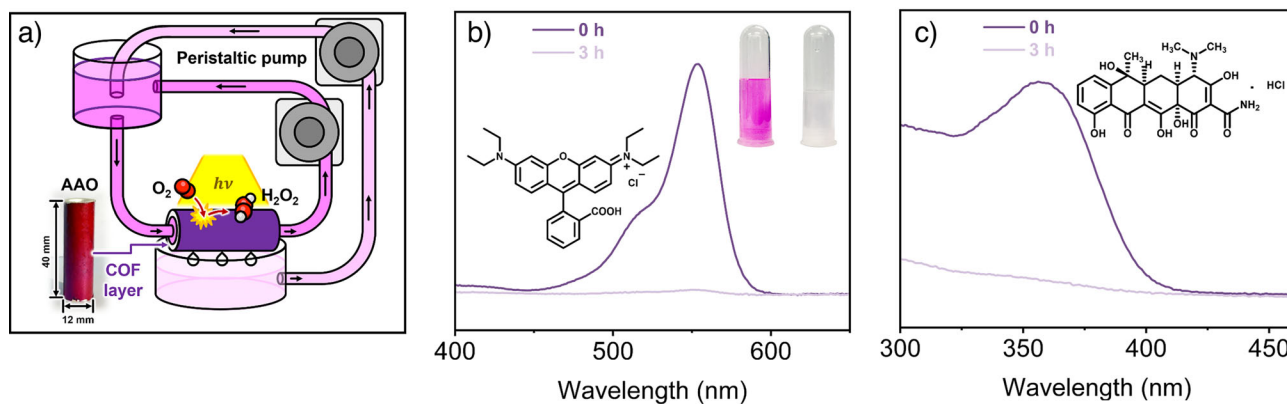


**Figure 6.** COF membrane reactor for organic pollutant degradation. a) Schematic illustration showing the integration of the COF-M180 membrane with tubular  $\text{Al}_2\text{O}_3$  for continuous organic pollutant degradation using in situ generated  $\text{H}_2\text{O}_2$ . Inset: Photograph of the COF-M180 and  $\text{Al}_2\text{O}_3$  composite membrane. b) and c) UV-vis spectra of Rhodamine B and tetracycline hydrochloride before and after degradation by the COF-M180 and  $\text{Al}_2\text{O}_3$  composite membrane under  $200 \text{ mW cm}^{-2}$  Xe lamp illumination.

The versatility of this approach is demonstrated through its application to various COF systems. For instance, membranes synthesized from 1,3,5-tris(4-aminophenyl)benzene (Tapb) paired with 2,5-divinylterephthalaldehyde (Dva) or 2-hydroxybenzene-1,3,5-tricarbaldehyde (Hta) (resulting in COF-TapbDva and COF-TapbHta) achieved  $\text{H}_2\text{O}_2$  production rates of  $18.4 \text{ mmol g}^{-1} \text{ h}^{-1}$  and  $5.0 \text{ mmol g}^{-1} \text{ h}^{-1}$  under  $200 \text{ mW cm}^{-2}$  Xe lamp irradiation, outperforming their powdered counterparts by 167- and 61-fold, respectively (Figures S40–S52). Collectively, these findings establish a robust framework for designing advanced photocatalysts that overcome mass transfer limitations, enabling scalable, efficient, and adaptable processes.

### Supporting Information

The authors have cited additional references within the Supporting Information.

### Acknowledgements

This work was supported by the National Key Research and Development Program of China (2022YFA1503004), National Science Foundation of China (22421004), and the National Science Foundation of Zhejiang province (LR23B060001 and LY23B060022). The authors appreciate the assistance of Fang Chen from Analytical Testing Center of the Department of Chemistry, Zhejiang University, in conducting SEM measurements.

### Conflict of Interests

The authors declare no conflict of interest.

### Data Availability Statement

The data that support the findings of this study are available in the Supporting Information of this article.

**Keywords:** Gas diffusion • Membrane catalysis • Photocatalytic  $\text{H}_2\text{O}_2$  synthesis • Triphase transport • Wettability control

- [1] S. C. Perry, D. Pangotra, L. Vieira, L.-I. Csepei, V. Sieber, L. Wang, C. Ponce De León, F. C. Walsh, *Nat. Rev. Chem.* **2019**, 3, 442–458, <https://doi.org/10.1038/s41570-019-0110-6>.
- [2] C. Xia, Y. Xia, P. Zhu, L. Fan, H. Wang, *Science* **2019**, 366, 226–231, <https://doi.org/10.1126/science.aay1844>.
- [3] Y. Liu, L. Li, Z. Sang, H. Tan, N. Ye, C. Sun, Z. Sun, M. Luo, S. Guo, *Nat. Synth.* **2024**, 4, 134–141, <https://doi.org/10.1038/s44160-024-00644-z>.
- [4] J. Zhang, P. Li, J. Yue, L. Meng, W. Li, C. Yang, S. Kim, Z. Cheng, A. Kamath, S. Siahrostami, B. Tian, *Nat. Nanotechnol.* **2025**, 20, 835–844, <https://doi.org/10.1038/s41565-025-01878-4>.
- [5] X. Zhang, Y. Wan, Y. Wen, Y. Zhu, H. Liu, J. Qiu, Z. Zhu, Z. Sun, X. Gao, S. Bai, Y. Zhang, L. Zhang, X. Yan, J. Zhang, Y. Liu, S. Li, L.-D. Zhao, *Nat. Catal.* **2025**, 8, 465–475, <https://doi.org/10.1038/s41929-025-01335-4>.
- [6] T. Freese, J. T. Meijer, B. L. Feringa, S. B. Beil, *Nat. Catal.* **2023**, 6, 553–558, <https://doi.org/10.1038/s41929-023-00980-x>.
- [7] S. J. Freakley, Q. He, J. H. Harrhy, L. Lu, D. A. Crole, D. J. Morgan, E. N. Ntainjua, J. K. Edwards, A. F. Carley, A. Y. Borisevich, C. J. Kiely, G. J. Hutchings, *Science* **2016**, 351, 965–968, <https://doi.org/10.1126/science.aad5705>.
- [8] H. Hou, X. Zeng, X. Zhang, *Angew. Chem. Int. Ed.* **2020**, 59, 17356–17376, <https://doi.org/10.1002/anie.201911609>.
- [9] H. Wang, C. Yang, F. Chen, G. Zheng, Q. Han, *Angew. Chem. Int. Ed.* **2022**, 61, e202202328, <https://doi.org/10.1002/anie.202202328>.
- [10] Y. Luo, B. Zhang, C. Liu, D. Xia, X. Ou, Y. Cai, Y. Zhou, J. Jiang, B. Han, *Angew. Chem. Int. Ed.* **2023**, 62, e202305355.
- [11] Y. Tang, W. Wang, J. Ran, C. Peng, Z. Xu, W. Chu, *Energ. Environ. Sci.* **2024**, 17, 6482–6498, <https://doi.org/10.1039/D4EE02505A>.
- [12] Z. Yong, T. Ma, *Angew. Chem. Int. Ed.* **2023**, 62, e202308980.
- [13] D. Chen, W. Chen, Y. Wu, L. Wang, X. Wu, H. Xu, L. Chen, *Angew. Chem. Int. Ed.* **2023**, 62, e202217479.
- [14] B. Mishra, A. Alam, A. Chakraborty, B. Kumbhakar, S. Ghosh, P. Pachfule, A. Thomas, *Adv. Mater.* **2024**, 36, 2413118, <https://doi.org/10.1002/adma.202413118>.
- [15] X. Yu, Z. Wei, Y. Qin, X. Zhang, D. Hao, L. Jing, Y. Liu, H. Dai, J. Deng, Y. Zhu, *Adv. Mater.* **2025**, 37, 2501494, <https://doi.org/10.1002/adma.202501494>.

- [16] C. Shu, X. Yang, L. Liu, X. Hu, R. Sun, X. Yang, A. I. Cooper, B. Tan, X. Wang, *Angew. Chem. Int. Ed.* **2024**, *63*, e202403926, <https://doi.org/10.1002/anie.202403926>.
- [17] Q. Zhi, W. Liu, R. Jiang, X. Zhan, Y. Jin, X. Chen, X. Yang, K. Wang, W. Cao, D. Qi, J. Jiang, *J. Am. Chem. Soc.* **2022**, *144*, 21328–21336, <https://doi.org/10.1021/jacs.2c09482>.
- [18] J. Sun, H. Sekhar Jena, C. Krishnaraj, K. Singh Rawat, S. Abednatanzi, J. Chakraborty, A. Laemont, W. Liu, H. Chen, Y. Liu, K. Leus, H. Vrielinck, V. Van Speybroeck, P. Van Der Voort, *Angew. Chem. Int. Ed.* **2023**, *62*, e202216719, <https://doi.org/10.1002/anie.202216719>.
- [19] D. Jiang, V. G. W. Tan, Y. Gong, H. Shao, X. Mu, Z. Luo, S. He, *Chem. Rev.* **2025**, *125*, 6203–6308, <https://doi.org/10.1021/acs.chemrev.4c00950>.
- [20] B. Luan, X. Chu, Y. Wang, X. Qiao, Y. Jiang, F. Zhang, *Adv. Mater.* **2024**, *36*, 2412653, <https://doi.org/10.1002/adma.202412653>.
- [21] Q. Li, J.-N. Chang, Z. Wang, M. Lu, C. Guo, M. Zhang, T.-Y. Yu, Y. Chen, S.-L. Li, Y.-Q. Lan, *J. Am. Chem. Soc.* **2023**, *145*, 23167–23175, <https://doi.org/10.1021/jacs.3c07471>.
- [22] R. Liu, Y. Chen, H. Yu, M. Položij, Y. Guo, T. C. Sum, T. Heine, D. Jiang, *Nat. Catal.* **2024**, *7*, 195–206, <https://doi.org/10.1038/s41929-023-01102-3>.
- [23] K. Endo, S. Canossa, F. Heck, D. M. Proserpio, M. S. Istek, F. Stemmler, J. Van Slageren, S. Hartmann, A. Hartschuh, B. V. Lotsch, *Nat. Synth.* **2025**, *4*, 603–613, <https://doi.org/10.1038/s44160-024-00719-x>.
- [24] P. Das, J. Roeser, A. Thomas, *Angew. Chem. Int. Ed.* **2023**, *62*, e202304349.
- [25] P. Das, G. Chakraborty, J. Roeser, S. Vogl, J. Rabeah, A. Thomas, *J. Am. Chem. Soc.* **2023**, *145*, 2975–2984, <https://doi.org/10.1021/jacs.2c11454>.
- [26] Y. Wang, R. Shi, L. Shang, G. I. N. Waterhouse, J. Zhao, Q. Zhang, L. Gu, T. Zhang, *Angew. Chem. Int. Ed.* **2020**, *59*, 13057–13062, <https://doi.org/10.1002/anie.202004841>.
- [27] Q. Zhang, M. Zhou, G. Ren, Y. Li, Y. Li, X. Du, *Nat. Commun.* **2020**, *11*, 1731, <https://doi.org/10.1038/s41467-020-15597-y>.
- [28] H. Zhou, X. Sheng, J. Xiao, Z. Ding, D. Wang, X. Zhang, J. Liu, R. Wu, X. Feng, L. Jiang, *J. Am. Chem. Soc.* **2020**, *142*, 2738–2743, <https://doi.org/10.1021/jacs.9b12247>.
- [29] A. K. Mohammed, A. A. Al Khoori, M. A. Addicoat, S. Varghese, I. Othman, M. A. Jaoude, K. Polychronopoulou, M. Baias, M. A. Haija, D. Shetty, *Angew. Chem. Int. Ed.* **2022**, *61*, e202200905, <https://doi.org/10.1002/anie.202200905>.
- [30] L. Fang, H. Xu, S. Qiu, T. Ye, T. Wang, J. Shang, C. Gu, S. Kitagawa, L. Li, *Angew. Chem. Int. Ed.* **2025**, *64*, e202423220.
- [31] L. Li, L. Xu, Z. Hu, J. C. Yu, *Adv. Funct. Mater.* **2021**, *31*, 2106120, <https://doi.org/10.1002/adfm.202106120>.
- [32] H. Huang, R. Shi, Z. Li, J. Zhao, C. Su, T. Zhang, *Angew. Chem. Int. Ed.* **2022**, *61*, e202200802, <https://doi.org/10.1002/anie.202200802>.
- [33] Y. Li, Z. Pei, D. Luan, X. W. D. Lou, *J. Am. Chem. Soc.* **2024**, *146*, 3343–3351, <https://doi.org/10.1021/jacs.3c12465>.
- [34] A. Li, Q. Cao, G. Zhou, B. V. K. J. Schmidt, W. Zhu, X. Yuan, H. Huo, J. Gong, M. Antonietti, *Angew. Chem. Int. Ed.* **2019**, *58*, 14549–14555, <https://doi.org/10.1002/anie.201908058>.
- [35] Y. Wu, J. Feng, H. Gao, X. Feng, L. Jiang, *Adv. Mater.* **2019**, *31*, 1800718, <https://doi.org/10.1002/adma.201800718>.
- [36] J. Chen, Z. Tang, L. Sheng, Z. Li, D. Zhu, J. Wang, Y. Tang, X. He, H. Xu, *J. Am. Chem. Soc.* **2025**, *147*, 3714–3723, <https://doi.org/10.1021/jacs.4c16029>.
- [37] X. Zhang, B. Tu, Z. Cao, M. Fang, G. Zhang, J. Yang, Y. Ying, Z. Sun, J. Hou, Q. Fang, Z. Tang, L. Li, *J. Am. Chem. Soc.* **2023**, *145*, 17786–17794, <https://doi.org/10.1021/jacs.3c04655>.
- [38] W. Jiang, J. Zhou, X. Zhong, M. Fang, J. Hao, D. Zhao, X. Wen, H. Wang, Y. Zhou, Y. Zhu, L. Jiang, *Nat. Sustain.* **2025**, *8*, 446–455, <https://doi.org/10.1038/s41893-024-01493-6>.
- [39] W. Weng, J. Guo, *J. Am. Chem. Soc.* **2024**, *146*, 13201–13209, <https://doi.org/10.1021/jacs.4c01097>.
- [40] Q. Liu, M. Liu, Z. Zhang, C. Yin, J. Long, M. Wei, Y. Wang, *Nat. Commun.* **2024**, *15*, 9221, <https://doi.org/10.1038/s41467-024-53625-3>.
- [41] F. Sheng, B. Wu, X. Li, T. Xu, M. A. Shehzad, X. Wang, L. Ge, H. Wang, T. Xu, *Adv. Mater.* **2021**, *33*, 2104404, <https://doi.org/10.1002/adma.202104404>.
- [42] Y. Yang, B. Liang, J. Kreie, M. Hamsch, Z. Liang, C. Wang, S. Huang, X. Dong, L. Gong, C. Liang, D. Lou, Z. Zhou, J. Lu, Y. Yang, X. Zhuang, H. Qi, U. Kaiser, S. C. B. Mannsfeld, W. Liu, A. Götzhäuser, Z. Zheng, *Nature* **2024**, *630*, 878–883, <https://doi.org/10.1038/s41586-024-07505-x>.
- [43] L. Cao, I.-C. Chen, C. Chen, D. B. Shinde, X. Liu, Z. Li, Z. Zhou, Y. Zhang, Y. Han, Z. Lai, *J. Am. Chem. Soc.* **2022**, *144*, 12400–12409, <https://doi.org/10.1021/jacs.2c04223>.
- [44] S. Zheng, X. Liu, C. Wang, Z. Ouyang, X. Zhang, S. Bi, G. Shi, Q. Xu, J. S. Francisco, G. Zeng, *J. Am. Chem. Soc.* **2025**, *147*, 15777–15786, <https://doi.org/10.1021/jacs.5c03492>.
- [45] S. Wang, Y. Fu, F. Wang, X. Wang, Y. Yang, M. Wang, J. Wang, E. Lin, H. Ma, Y. Chen, P. Cheng, Z. Zhang, *J. Am. Chem. Soc.* **2024**, *146*, 33509–33517, <https://doi.org/10.1021/jacs.4c10879>.
- [46] H. Yang, H. Zhang, C. Kang, C. Ji, D. Shi, D. Zhao, *Sci. Adv.* **2024**, *10*, eads0260, <https://doi.org/10.1126/sciadv.ads0260>.
- [47] M. Wang, P. Zhang, X. Liang, J. Zhao, Y. Liu, Y. Cao, H. Wang, Y. Chen, Z. Zhang, F. Pan, Z. Zhang, Z. Jiang, *Nat. Sustain.* **2022**, *5*, 518–526, <https://doi.org/10.1038/s41893-022-00870-3>.
- [48] J. Liu, S. Wang, T. Huang, P. Manchanda, E. Abou-Hamad, S. P. Nunes, *Sci. Adv.* **2020**, *6*, eabb3188, <https://doi.org/10.1126/sciadv.abb3188>.
- [49] X. Liu, W. Lin, K. Bader Al Mohawes, N. M. Khashab, *Angew. Chem. Int. Ed.* **2025**, *64*, e202419034.
- [50] R. Wang, Y. Zhou, Y. Zhang, J. Xue, J. Caro, H. Wang, *Adv. Mater.* **2022**, *34*, 2204894, <https://doi.org/10.1002/adma.202204894>.
- [51] J. Chen, M. Liu, Y. Liu, S. Shang, W. Gao, X. Wang, J. Hong, H. Xu, C. Hua, Z. You, Z. Zhou, S. Guo, Y. Liu, Y. Xu, *Angew. Chem. Int. Ed.* **2025**, *64*, e202505491.
- [52] W. Li, W. Duan, G. Liao, F. Gao, Y. Wang, R. Cui, J. Zhao, C. Wang, *Nat. Commun.* **2024**, *15*, 6763, <https://doi.org/10.1038/s41467-024-51183-2>.
- [53] T. Zhang, S. Chen, P. S. Petkov, P. Zhang, H. Qi, N. N. Nguyen, W. Zhang, J. Yoon, P. Li, T. Brumme, A. Alfonso, Z. Liao, M. Hamsch, S. Xu, L. Mester, V. Kataev, B. Büchner, S. C. B. Mannsfeld, E. Zschech, S. S. P. Parkin, U. Kaiser, T. Heine, R. Dong, R. Hillenbrand, X. Feng, *Nature* **2025**, *638*, 411–417, <https://doi.org/10.1038/s41586-024-08387-9>.
- [54] Y. Wang, P. Du, H. Pan, L. Fu, Y. Zhang, J. Chen, Y. Du, N. Tang, G. Liu, *Adv. Mater.* **2019**, *31*, 1807540, <https://doi.org/10.1002/adma.201807540>.
- [55] S. Gao, Q. Zhang, X. Su, X. Wu, X.-G. Zhang, Y. Guo, Z. Li, J. Wei, H. Wang, S. Zhang, J. Wang, *J. Am. Chem. Soc.* **2023**, *145*, 9520–9529, <https://doi.org/10.1021/jacs.2c11146>.
- [56] Z. Zhang, Y. Xu, *J. Am. Chem. Soc.* **2023**, *145*, 25222–25232, <https://doi.org/10.1021/jacs.3c08220>.
- [57] S. Zhao, C. Jiang, J. Fan, S. Hong, P. Mei, R. Yao, Y. Liu, S. Zhang, H. Li, H. Zhang, C. Sun, Z. Guo, P. Shao, Y. Zhu, J. Zhang, L. Guo, Y. Ma, J. Zhang, X. Feng, F. Wang, H. Wu, B. Wang, *Nat. Mater.* **2021**, *20*, 1551–1558, <https://doi.org/10.1038/s41563-021-01052-w>.
- [58] P. Dong, X. Xu, T. Wu, R. Luo, W. Kong, Z. Xu, S. Yuan, J. Zhou, J. Lei, *Angew. Chem. Int. Ed.* **2024**, *63*, e202405313, <https://doi.org/10.1002/anie.202405313>.
- [59] Y. Zhang, C. Pan, G. Bian, J. Xu, Y. Dong, Y. Zhang, Y. Lou, W. Liu, Y. Zhu, *Nat. Energy* **2023**, *8*, 361–371, <https://doi.org/10.1038/s41560-023-01218-7>.

- [60] C. Sun, Y. Han, H. Guo, R. Zhao, Y. Liu, Z. Lin, Z. Xiao, Z. Sun, M. Luo, S. Guo, *Adv. Mater.* **2025**, *37*, 2502990, <https://doi.org/10.1002/adma.202502990>.
- [61] H. Lin, Y. Yang, B. G. Diamond, T.-H. Yan, V. I. Bakhmutov, K. W. Festus, P. Cai, Z. Xiao, M. Leng, I. Afolabi, G. S. Day, L. Fang, C. H. Hendon, H.-C. Zhou, *J. Am. Chem. Soc.* **2024**, *146*, 1491–1500, <https://doi.org/10.1021/jacs.3c10917>.
- [62] R. Chen, Y. Wang, Y. Ma, A. Mal, X.-Y. Gao, L. Gao, L. Qiao, X.-B. Li, L.-Z. Wu, C. Wang, *Nat. Commun.* **2021**, *12*, 1354, <https://doi.org/10.1038/s41467-021-21527-3>.
- [63] X. Zhang, H. Liu, L. Jiang, *Adv. Mater.* **2019**, *31*, 1804508, <https://doi.org/10.1002/adma.201804508>.
- [64] W. Zhao, P. Yan, H. Yang, M. Bahri, A. M. James, H. Chen, L. Liu, B. Li, Z. Pang, R. Clowes, N. D. Browning, J. W. Ward, Y. Wu, A. I. Cooper, *Nat. Synth.* **2022**, *1*, 87–95, <https://doi.org/10.1038/s44160-021-00005-0>.
- [65] J. Yue, L. Song, Y. Fan, Z. Pan, P. Yang, Y. Ma, Q. Xu, B. Tang, *Angew. Chem. Int. Ed.* **2023**, *62*, e202309624.
- [66] Y.-X. Song, Z. Wang, Y.-H. Zhang, *J. Colloid Interf. Sci.* **2025**, *686*, 348–358, <https://doi.org/10.1016/j.jcis.2025.01.247>.
- [67] W. Xian, X. Xu, Y. Ge, Z. Xing, Z. Lai, Q.-W. Meng, Z. Dai, S. Wang, R. Chen, N. Huang, S. Ma, Q. Sun, *J. Am. Chem. Soc.* **2024**, *146*, 33973–33982, <https://doi.org/10.1021/jacs.4c12829>.
- [68] L. Liu, M.-Y. Gao, H. Yang, X. Wang, X. Li, A. I. Cooper, *J. Am. Chem. Soc.* **2021**, *143*, 19287–19293, <https://doi.org/10.1021/jacs.1c09979>.
- [69] D. Wang, F. Tan, W. Zhao, S. Zhou, Q. Xu, L. Kan, L. Zhu, P. Gu, J. Lu, *Angew. Chem. Int. Ed.* **2025**, *64*, e202425017.
- [70] W. Wu, Z. Li, S. Liu, D. Zhang, B. Cai, Y. Liang, M. Wu, Y. Liao, X. Zhao, *Angew. Chem. Int. Ed.* **2024**, *63*, e202404563, <https://doi.org/10.1002/anie.202404563>.
- [71] L. Guo, L. Gong, Y. Yang, Z. Huang, X. Liu, F. Luo, *Angew. Chem. Int. Ed.* **2025**, *64*, e202414658.
- [72] Q. Xue, H. Li, P. Jin, X. Zhou, F. Wang, *Angew. Chem. Int. Ed.* **2025**, *64*, e202423368.
- [73] R. Sun, X. Yang, X. Hu, Y. Guo, Y. Zhang, C. Shu, X. Yang, H. Gao, X. Wang, I. Hussain, B. Tan, *Angew. Chem. Int. Ed.* **2025**, *64*, e202416350, <https://doi.org/10.1002/anie.202416350>.
- [74] Z. Zhang, Y. Hou, S. Zhu, L. Yang, Y. Wang, H. Yue, H. Xia, G. Wu, S. Yang, X. Liu, *Angew. Chem. Int. Ed.* **2025**, *64*, e202505286, <https://doi.org/10.1002/anie.202505286>.
- [75] J. Chen, S. Yan, F. Wang, F. Lin, J. Lin, R. A. Borse, Y. Wang, *Angew. Chem. Int. Ed.* **2025**, *64*, e202500924, <https://doi.org/10.1002/anie.202500924>.
- [76] J. Liu, C. Tuo, W. Xiao, M. Qi, Y. Yusran, Z. Wang, H. Li, C. Guo, J. Song, S. Qiu, Y. Xu, Q. Fang, *Angew. Chem. Int. Ed.* **2025**, *64*, e202416240, <https://doi.org/10.1002/anie.202416240>.
- [77] H. Yan, Y. Huang, M. Shen, J. Xu, Y. Ye, G. Ouyang, *Angew. Chem. Int. Ed.* **2025**, *64*, e202425054, <https://doi.org/10.1002/anie.202425054>.
- [78] J.-H. Zhang, Z.-M. Ge, J. Wang, D.-C. Zhong, T.-B. Lu, *Nat. Commun.* **2025**, *16*, 2448, <https://doi.org/10.1038/s41467-025-57939-8>.
- [79] Q. Zhang, K. Gu, C. Dong, C. Xue, H. Che, K. Zhang, Y. Ao, *Angew. Chem. Int. Ed.* **2025**, *64*, e202417591.
- [80] W. Li, B. Han, Y. Liu, J. Xu, H. He, G. Wang, J. Li, Y. Zhai, X. Zhu, Y. Zhu, *Angew. Chem. Int. Ed.* **2025**, *64*, e202421356, <https://doi.org/10.1002/anie.202421356>.
- [81] Y. Peng, L. Yuan, K. Liu, Z. Guan, S. Jin, Y. Fang, *Angew. Chem. Int. Ed.* **2025**, *64*, e202423055.
- [82] Z.-Q. Wang, M.-H. Li, S. Liang, Y. Kong, C. Wang, L. Li, J.-J. Xu, Y.-W. Yang, *J. Am. Chem. Soc.* **2025**, *147*, 13618–13628, <https://doi.org/10.1021/jacs.5c00768>.
- [83] Y. Luo, B. Zhang, C. Liu, D. Xia, X. Ou, Y. Cai, Y. Zhou, J. Jiang, B. Han, *Angew. Chem. Int. Ed.* **2023**, *62*, e202305355.

Manuscript received: September 05, 2025

Revised manuscript received: October 09, 2025

Manuscript accepted: October 14, 2025

Version of record online: October 25, 2025